

# Analysis and interpretation of instantaneous turbulent velocity fields

R. J. Adrian, K. T. Christensen, Z.-C. Liu

275

**Abstract** Methods of analyzing and interpreting velocity-field data (both two- and three-dimensional) to understand the kinematics, dynamics, and scales of turbulence are discussed. Reynolds decomposition and vorticity are traditionally used; however, several other methods, including Galilean (constant convection velocity) and LES decompositions (low-pass filtering), in conjunction with critical-point analysis of the local velocity gradient tensor, reveal more about the structure of turbulence. Once the small-scale structures have been identified, it is necessary to assess their importance to the overall dynamics of the turbulence by visualizing the motions they induce and the stresses they impose both on other small-scale vortices and on the larger-scale field.

## List of symbols

$a$	coefficients of POD expansion
$\underline{\underline{D}}^{2-D}$	two-dimensional local velocity gradient tensor, $= \partial u_i / \partial x_j$ , $i, j = 1, 2$
$f$	filtering kernel
$H$	characteristic function of POD filter
$k = 2\pi/\lambda$	wavenumber
$P$	mean pressure
$Q_i$	$i$ th quadrant of the $u'_1 - u'_2$ plane
$R$	pipe radius
$Re_D$	Reynolds number based on pipe diameter and bulk streamwise velocity
$\mathbf{u} = (u_1, u_2, u_3)$	total velocity
$\mathbf{U} = (U_1, U_2, U_3)$	mean velocity
$\mathbf{u}' = \mathbf{u} - \mathbf{U}$	Reynolds-decomposed velocity fluctuation
$\bar{\mathbf{u}}$	LES-decomposed large-scale (filtered) field

$\mathbf{u}'' = \mathbf{u} - \bar{\mathbf{u}}$
$\mathbf{U}_c$
$\mathbf{u}_c = \mathbf{u} - \mathbf{U}_c$
$u_* = \sqrt{\tau_w/\rho}$
$U_{CL}$
$\mathbf{x} = (x_1, x_2, x_3)$
$y_* = \mu/(\rho u_*)$

LES-decomposed velocity fluctuation
Galilean convection velocity
Galilean-decomposed velocity fluctuation
wall-friction velocity
centerline velocity
spatial coordinate
viscous length scale

## Greek symbols

$\phi_i$	optimal, inhomogeneous POD basis function for the $i$ th component of velocity
$\eta$	Kolmogorov length scale
$\lambda_{ci}$	swirling strength (imaginary portion of the complex eigenvalue of the local velocity gradient tensor)
$\mu$	dynamic viscosity
$\psi_i$	orthogonal basis for $i$ th component of velocity
$\rho$	density
$\tau_w$	wall shear-stress
$\omega$	frequency ( $\text{rad} \cdot \text{s}^{-1}$ )
$\boldsymbol{\omega}$	vorticity

## Subscripts

1	streamwise direction
2	wall-normal (radial) direction

## Superscripts

+	viscous wall units
---	--------------------

## 1

### Introduction

Over the past fifteen years of turbulence research, the amount of information obtained through the application of new experimental and computational tools has grown immensely. The two-dimensional (2-D) velocity vector fields obtained by particle image velocimetry (PIV) and the three-dimensional (3-D) fields obtained by direct numerical simulation (DNS), large eddy simulation (LES) and holographic PIV (HPIV) provide new insight into the scales, kinematics, and dynamics of turbulence and demand new methods of extracting this information and interpreting it properly. These methods *must* take advantage of the quantitative nature of the data.

Received: 31 May 1999/Accepted: 24 October 1999

R.J. Adrian, K.T. Christensen, Z.-C. Liu  
Laboratory for Turbulence and Complex Flow  
Department of Theoretical and Applied Mechanics  
University of Illinois, Urbana, IL 61801, USA

Correspondence to: R.J. Adrian

This research was supported by NSF-ATM grant number 95-22662 and NSF-CTS grant number 96-16219. One of the authors (KTC) was supported by an NSF Graduate Fellowship. The authors gratefully acknowledge C.D. Meinhart for allowing us to use his pipe-flow PIV data as an example in this paper.

Reynolds decomposition into mean and fluctuating portions is the de facto standard method of describing turbulent velocity fields. While the fluctuating fields found by Reynolds decomposition are the correct basis for the analysis of statistics, they do not always constitute the best method for visualizing the turbulent mechanics of a flow. The method that is best suited to a particular investigation is determined by the questions one asks. If the ultimate goal is to understand statistical interrelationships so as to contribute to improved Reynolds-averaged Navier–Stokes models, then Reynolds decomposition is the correct choice. However, if one wishes to focus on the dynamics of small-scale vortices, or on the contribution of small structures to the stresses acting on larger structures, then methods that unambiguously detect small eddies may be better suited. Alternatively, if one wishes to understand the structured, coherent elements of the flow, then methods of visualization that leave the large structures intact may be more appropriate.

While the foregoing considerations seem quite apparent, the use of Reynolds decomposition is so widespread and so ingrained in the turbulence community that it is used almost universally, regardless of its suitability for a particular purpose. A primary goal of this paper is to discuss several other decomposition methods and to articulate their uses in addressing various questions about turbulence.

The issue of identifying vortices in a flow field first arose with the advent of flow visualization techniques (dye injection, smoke-wire, etc.). The patterns created by these techniques represent streaklines. Hama (1962) showed that streaklines observed in a shear flow perturbed by a traveling sinusoidal wave of constant amplitude can roll-up, falsely indicating the presence of discrete vortices. Gursul et al. (1990) argue that it is crucial to choose the correct reference frame in which to visualize streakline patterns because a steady flow can appear unsteady in an incorrect frame of reference. These two examples serve to indicate that visualization of vortices using streaklines may be ambiguous. This is because streaklines represent traces of particle images over both a limited portion of the flow and a long-time interval. Velocity vector fields, on the other hand, cover the entire field and represent motion over a very short time. We shall see, however, that interpretation of velocity vector fields also requires care.

Identification of vortices in a velocity field, along with calculation of vortex statistics (i.e., diameter, strength, etc.), is normally accomplished by identifying isolated ‘regions’ of significant vorticity (vortex ‘cores’) (see, for example, Jiménez et al., 1993). In simple flows with minimal shear, this task is relatively straightforward. However, in complex flow fields, this is not the case. Vortices are often ‘masked’ by regions of significant shear, making it nearly impossible to obtain reliable vortex statistics. In this case, it is extremely difficult to use vorticity maps to identify vortices and to assess their contribution to the overall flow.

This paper provides new methods for extracting information from velocity fields about the scales, kinematics, and dynamics of turbulence. These ideas are also appropriate for other complex flows in general, but the

focus of this paper will be on turbulence, wherein some of the greatest challenges lie. Specifically, we wish to identify small-scale vortices and determine their contribution to the overall dynamics of the flow. Alternative methods to Reynolds averaging include decomposition by Galilean transformation and by filtered fields, as in LES. This filtering can be homogeneous (a Gaussian filter, for example) or inhomogeneous (as in proper orthogonal decomposition (POD)). These particular methods separate the field based on the scale of the fluid motions in space or time. Yet another class of decompositions is based on classifying points in the turbulent field according to a certain property (or group of properties), such as rotation. The field is then decomposed into regions based on the magnitude of that property. A classic example of this is to separate the velocity field into toroidal and poloidal fields. Modern eddy classifiers (swirling strength analysis) based on critical-point analysis of the local velocity gradient tensor will also be discussed and compared to vorticity.

## 2

### Decomposition by scale

Decomposition by scale denotes separating the total vector field into portions having different scales of length or time. For example, let  $\mathbf{u}$  be the total velocity vector and let

$$\mathbf{U}(\mathbf{x}, t) \equiv \langle \mathbf{u} \rangle \quad (1)$$

be the mean of the total velocity, defined either by ensemble averaging, time averaging or spatially averaging in a statistically homogeneous direction. The Reynolds decomposition

$$\mathbf{u} = \mathbf{U} + \mathbf{u}' \quad (2)$$

can then be viewed as a scale decomposition in several ways, depending upon the definition of the mean. If the mean is determined by long-time averaging, the decomposition separates the field into a (possibly position dependent) component that has infinite time-scale and a fluctuation that contains all other components of lesser time-scale. If the mean is found by averaging in one or more spatial directions, then the mean may vary both in time and in the non-averaging directions, and the decomposition separates the field into a component that has infinite scale in the averaging directions and a component that fluctuates on finite spatial scales and in time. Note that either approach is extreme because, out of the full space-time spectrum of motions, the decomposition only isolates the component that has infinite scale from all others. This is illustrated graphically in Fig. 1. One can easily question the singular importance of  $k = 0$  or  $\omega = 0$ , as opposed to isolating the components that are merely large-scale in space and/or time.

A more general approach is to define a decomposition by separating the space-time spectrum of the field into two or more groups, each representing different aspects of the field (Fig. 1). Separation done purely in space is essentially the approach of LES decomposition. The large-eddy field is defined by low-pass filtering the total velocity as

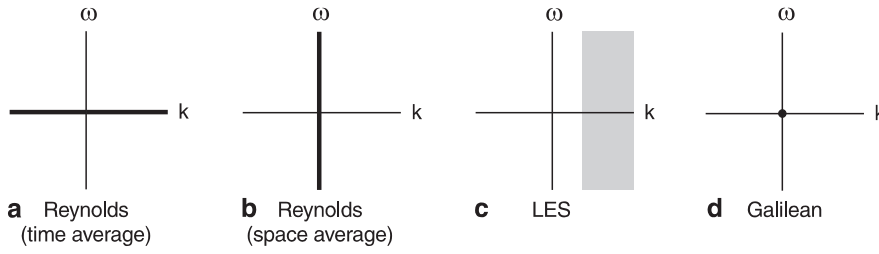


**Fig. 1a–d.** Illustration of various scale decompositions in wave space. **a** Reynolds (time average); **b** Reynolds (space average); **c** LES; **d** Galilean

$$\bar{\mathbf{u}}(\mathbf{x}, t) = \int_D f(\mathbf{x}, \mathbf{x}') \mathbf{u}(\mathbf{x}', t) d\mathbf{x}' \quad (3)$$

to obtain the filtered (large-scale) field,  $\bar{\mathbf{u}}$  ( $f$  is the filtering kernel and  $D$  is the domain of the velocity field). If the filtering kernel is shift-invariant (i.e., homogeneous) then  $f(\mathbf{x}, \mathbf{x}')$  can be simplified to  $f(\mathbf{x} - \mathbf{x}')$ . The total field is the sum of the large-scale field and the remaining smaller-scale field

$$\mathbf{u} = \bar{\mathbf{u}} + \mathbf{u}'' \quad (4)$$

This type of decomposition is extremely useful in visualizing small-scale turbulent eddies because it removes the translation imposed by the larger-scale field on the small-scale vortices. Note that the filtering kernel,  $f$ , can either be defined using a standard homogeneous filter (Gaussian, top-hat, etc.) or by inhomogeneous filters for inhomogeneous flows. The use of POD to define an inhomogeneous filter will be discussed in Sect. 3.3.

Galilean transformation is the simplest method of decomposition, although not one that necessarily involves scale decomposition. The total velocity is represented as the sum of a constant convection velocity,  $\mathbf{U}_c$ , plus the deviation

$$\mathbf{u} = \mathbf{U}_c + \mathbf{u}_c \quad (5)$$

If the convection velocity is a freely-selected constant, the Galilean transformation removes a constant that is independent of space and time, i.e.  $k = \omega = 0$  (Fig. 1). However, if  $\mathbf{U}_c$  is found by averaging over a local region, then the convection velocity corresponds to a moving average, which has the properties of a low-pass filter. In PIV, the measured vector field is often averaged over the entire field of view, and this value is then subtracted from the total field before displaying it.

As mentioned earlier, the choice of decomposition method can have a dramatic effect on the visualization of the resulting fluctuating field. In the coming sections, we will consider these effects on the visualization of both small-scale vortices and the events that contribute to the turbulent (Reynolds) stresses.

### 3

#### Visualization of vortices

It has been surprisingly challenging for the fluid dynamics community to arrive at a consensus definition of a vortex or an eddy, as evidenced by the many proposals one can find in the recent research literature (Chong et al., 1990; Dallman et al., 1991; Jeong and Hussain, 1995; Zhou et al., 1996, 1999; among others). While a widely accepted defi-

nition does not currently exist, the various methods that have been proposed all arrive at broadly similar results. For the present, it is sufficient to refer to the definition offered by Kline and Robinson (1989) and Robinson et al. (1989): “A vortex exists when instantaneous streamlines mapped onto a plane normal to the core exhibit a roughly circular or spiral pattern, when viewed in a reference frame moving with the center of the vortex core”. A key condition in this definition is that the velocity field must be viewed in a frame that moves at the same velocity as the core of the vortex. A second key condition is that the vorticity is concentrated in a “core”. If a turbulent field consists of large-scale motion with many small-scale vortices embedded within it, it will only be possible to recognize a vortex in terms of the foregoing definition if the velocity at the center of each small vortex is removed. An important function of decomposition by scale is to do exactly this. Galilean analysis can also reveal most of the vortex cores in a flow field if one systematically cycles through a range of convection velocities. At each convection velocity one sees the vortices propagating at that velocity.

Figure 2 illustrates the effect of convection velocity on the visualization of a turbulent eddy. Removing a velocity which is less than the translational velocity of the vortex is shown in Fig. 2a. Since the streamlines are not closed, by the definition of Kline and Robinson (1989), the vortex is not properly visualized. The true frame of reference of the vortex is shown in Fig. 2b. Finally, overestimation of the convection velocity of the vortex again results in open streamlines, Fig. 2c. This technique is consistent with the spirit of Michalke (1964). It is also helpful, as a secondary check, to “confirm” the existence of an eddy by comparing the location of the apparent center of the closed streamlines to the maximum in the local concentration of vorticity or swirling strength (see Sect. 3.4).

To illustrate these ideas, we will use a typical PIV realization in the radial-streamwise plane of fully-developed turbulent pipe flow as an example. This particular realization is part of an ensemble of photographic PIV measurements made at a Reynolds number  $Re_D = 50,000$  (viscous length scale  $y_* = 50\text{-}\mu\text{m}$ , non-dimensional pipe radius (in viscous wall units)  $R^+ = 1300$ , and centerline velocity  $U_{CL} = 7.7\text{ m/s}$ ) by Urushihara et al. (1993). Velocity data extends nearly 500 viscous wall units in the streamwise direction ( $x_1^+$ ) and over 250 viscous wall units in the radial direction ( $x_2^+$ ). A block of data in the upper left-hand corner of the field has been removed due to severe laser flare from the pipe wall. The PIV photographs

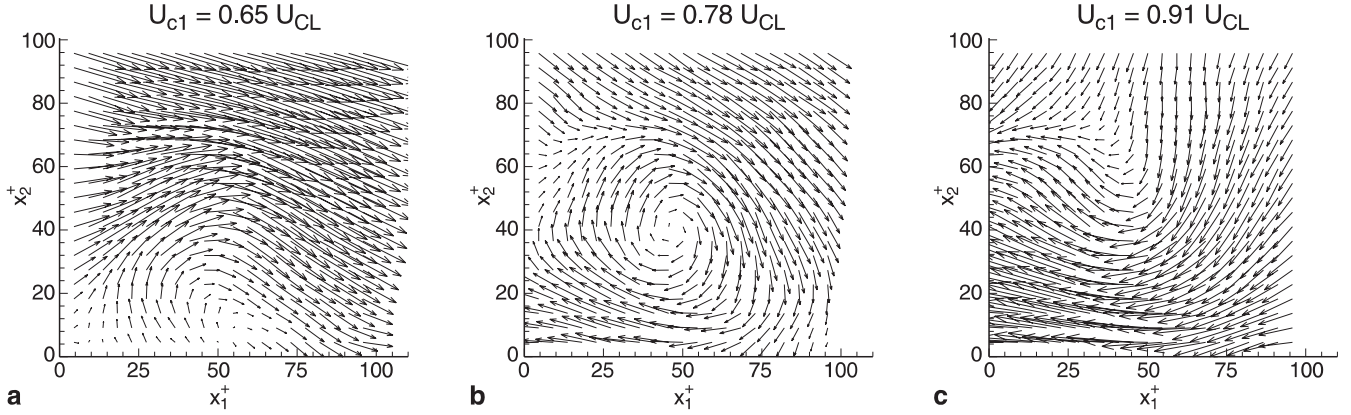


**Fig. 2a–c.** Visualization of an isolated turbulent eddy by Galilean decomposition for three different convection velocities: **a**  $U_{c1} = 0.65 U_{CL}$ ; **b**  $U_{c1} = 0.78 U_{CL}$ ; **c**  $U_{c1} = 0.91 U_{CL}$ .  $U_{c1} = 0.78$

$U_{CL}$  is the ‘correct’ convection velocity based upon the Kline and Robinson (1989) definition

were interrogated using  $454\text{-}\mu\text{m} \times 454\text{-}\mu\text{m}$  interrogation spots with 50% overlap, yielding a grid spacing of  $227\text{-}\mu\text{m}$  in each direction (4.6 viscous wall units). This high spatial resolution permitted resolution of vortices as small as four Kolmogorov scales ( $\eta^+ = 2.4$ ; volume-averaged) using three points across the diameter of the vortex.

### 3.1

#### Galilean decomposition

In this section, we illustrate the visualization of small-scale vortices by Galilean decomposition. The aforementioned field is shown in Fig. 3a–c with three different streamwise convection velocities ( $U_{c1}$ ) removed:  $U_{c1} = 0.5 U_{CL}$ ,  $0.75 U_{CL}$  and  $0.81 U_{CL}$ , respectively. The visible vortices are labeled A–I. Each value of the convection velocity corresponds to a different translational velocity of groups of vortices embedded within the flow. When the convection velocity matches an eddy’s translational velocity, it becomes recognizable as a roughly circular pattern of velocity vectors as defined by Kline and Robinson (1989).

For  $U_{c1} = 0.5 U_{CL}$  (Fig. 3a), five vortices near the wall ( $x_2^+ < 60$ ) are exposed (A–E). The vortices in this example lie just above the interface between the buffer and logarithmic regions of the wall layer. In addition, a large region of relatively uniform momentum (darkened portion of the velocity map) is exposed (roughly between  $100 < x_1^+ < 300$  and  $100 < x_2^+ < 250$ ).

For  $U_{c1} = 0.75 U_{CL}$  (Fig. 3b), two additional vortices (F, G) are revealed further away from the wall ( $50 < x_2^+ < 100$ ), along with vortex D, which was also seen in the previous case (although its apparent center has moved slightly further away from the wall in this frame). The fact that D is still recognizable as a vortex in this frame of reference shows that it is not necessary to remove an eddy’s exact translational velocity in order to visualize it. This particular value of convection velocity happens to correspond to the frame-averaged streamwise velocity. The  $Q_2$  events induced by the vortices near the wall are also visualized ( $0 < x_1^+ < 470$  and  $x_2^+ < 70$ ). In the analysis of turbulent shear flows with

mean shear  $\partial U_1 / \partial x_2$ , fluctuating velocity vectors lying in the second quadrant of the  $u'_1$ – $u'_2$  plane are referred to as  $Q_2$  events (i.e.,  $u'_1 < 0$ ,  $u'_2 > 0$ ). They transport low-momentum fluid away from the wall, and they contribute to the mean, negative values of the Reynolds shear stress,  $\langle u'_1 u'_2 \rangle$ . An outer region vortex (H) is partially evident in this frame of reference; however, its velocity vector pattern is not completely circular, implying that this is not quite the most appropriate frame in which to visualize it. Additionally, the uniform momentum zone in the outer region of the field discussed in the previous case is still visible at this convection velocity.

Finally, for  $U_{c1} = 0.81 U_{CL}$  (Fig. 3c), a new outer region ( $x_2^+ > 200$ ) vortex becomes visible (I), along with those already seen in Fig. 3b (D, F–H). The vortex H has become much more circular in this reference frame as compared to the previous one. The uniform momentum zone in the outer region is less visible in this frame of reference, although the  $Q_2$  events near the wall are still quite strong. It is evident from this discussion that one must consider a range of convection velocities in order to identify the majority of the turbulent eddies embedded in a velocity field.

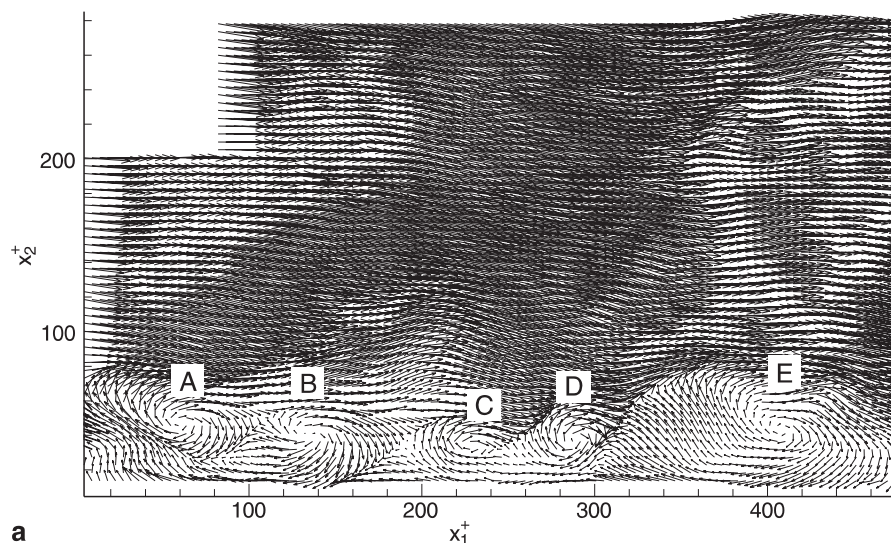
### 3.2

#### Reynolds decomposition

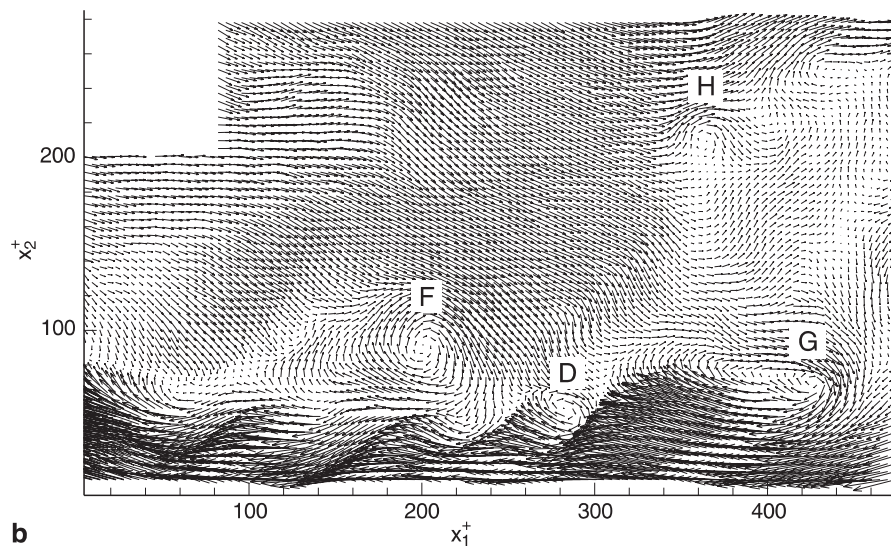
As mentioned previously, Reynolds decomposition is the traditional method of decomposing a turbulent velocity field. Reynolds decomposition of the pipe flow example (Fig. 4a) reveals six of the vortices (A–E, H), mostly near the wall. Reynolds decomposition tends to reveal more vortices than any single Galilean decomposition because the vortices frequently move at velocities close to the local mean velocity. Therefore, by subtracting the mean velocity profile,  $U(x_2^+)$ , many more vortices are visualized than by removing a single convection velocity. One of the strengths of Reynolds decomposition is that it does a fair job of revealing the small-scale vortices.

One of the weaknesses of Reynolds decomposition is that it removes large-scale features (mechanisms) that

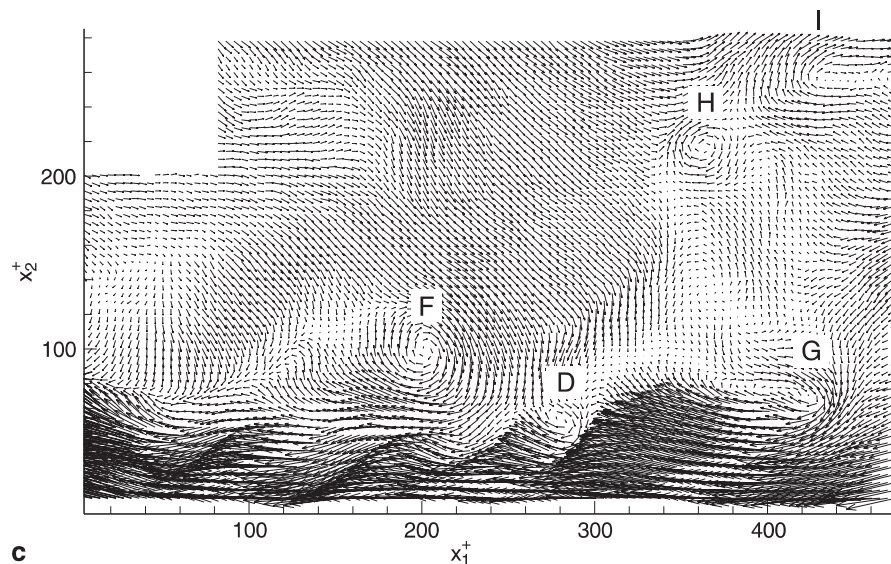




a



b



c

**Fig. 3a–c.** Fluctuating vector fields in pipe flow found by Galilean decomposition. **a**  $U_{c1} = 0.5 U_{CL}$ ; **b**  $U_{c1} = 0.75 U_{CL}$ ; **c**  $U_{c1} = 0.81 U_{CL}$ . The small-scale vortices are labeled A–I

are intimately associated with the mean flow. Thus, comparing Fig. 3 to Fig. 4a, one sees the large region of relatively uniform momentum in the Galilean

decomposition is not as visible in the Reynolds-decomposed field. In addition, the  $Q_2$  events associated with the vortices are less visible in the Reynolds de-

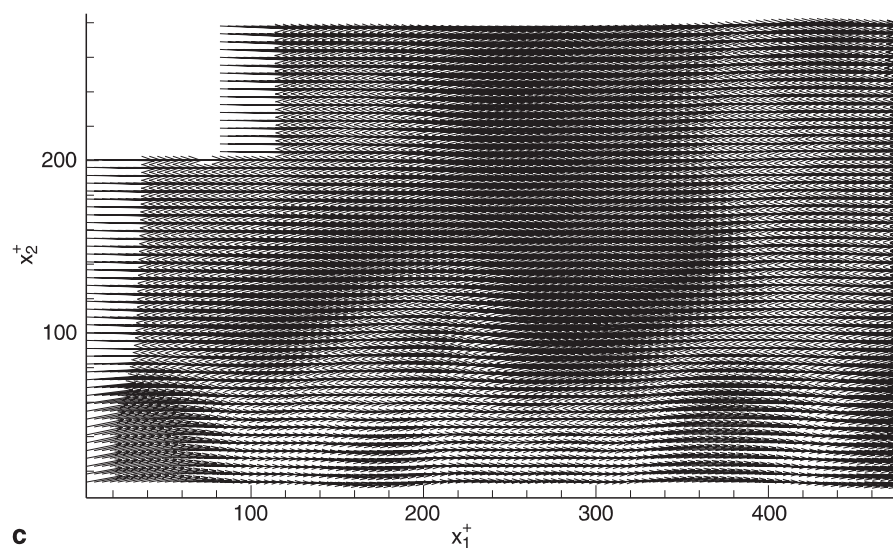
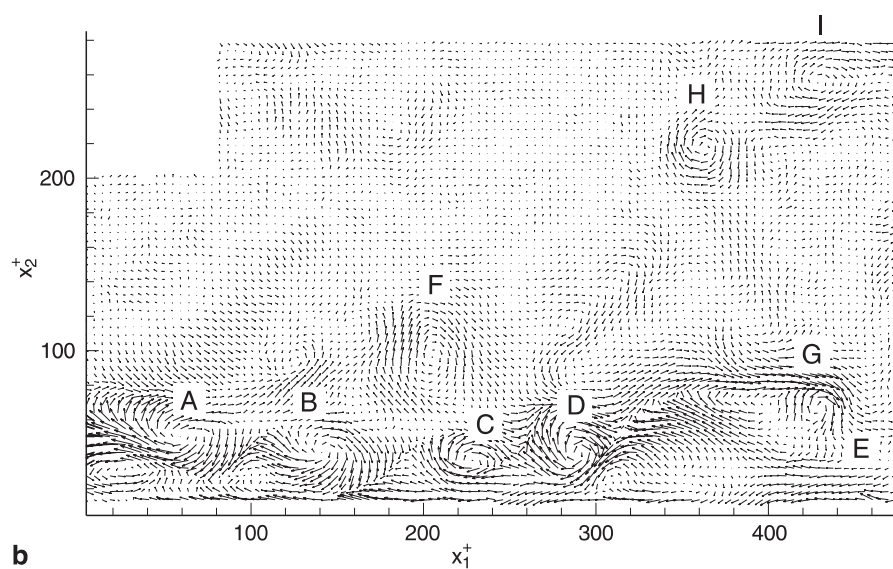
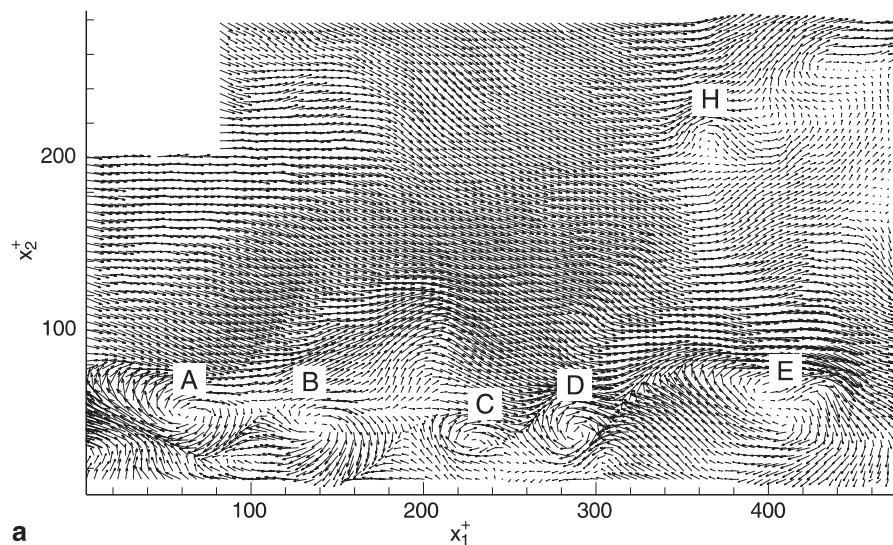


**Fig. 4a-c.** Pipe flow velocity fields illustrating **a** Reynolds-decomposed fluctuations; **b** LES-decomposed fluctuations; **c** LES low-pass filtered field

composition. These regions provide important clues to the structure of the logarithmic layer (Meinhart and Adrian 1995). In Figs. 3b and 4a, the uniform mo-

mentum zones are about equally visible; however, the  $Q_2$  events close to the wall are obscured by the Reynolds decomposition.

### 3.3 LES decomposition

#### 3.3.1 Homogeneous filtering

If the small-scale vortices translate with the velocity of the larger-scale vortices in which they are embedded, then the small-scale field obtained by LES decomposition should reveal all of the recognizable small-scale eddies in the field (Since the data in our example is planar PIV data, the vortices must also have axes roughly perpendicular to the plane in order to be recognized. Vortices making any angle appear as ellipses and those making angles greater than  $\pm 60^\circ$  are often difficult to identify). In this study, a homogeneous Gaussian filter was used to compute the filtered field. Figure 4b shows the LES-decomposed small-scale velocity field ( $\mathbf{u}''$ ) for our pipe flow example. It was obtained by subtracting the filtered field ( $\bar{\mathbf{u}}$ ) from the total velocity field. As expected, the small-scale field reveals eddies from all three of the layers noted in Fig. 3, indicating that it is superior to both Reynolds and Galilean decomposition as an eddy visualization tool. Note that the LES fluctuating field does not provide any insight into regions of constant momentum. However, the filtered field itself should show the large-scale features of the flow, i.e. the uniform momentum zones. In Fig. 4c, regions of near-constant momentum are evident for  $100 < x_1^+ < 375$  and  $x_2^+ > 100$ . These coincide well with those seen in the Galilean decompositions, especially Fig. 3a.

#### 3.3.2 Inhomogeneous filtering (proper orthogonal decomposition)

One of the problems with using homogeneous filtering in a turbulent flow field that has statistically inhomogeneous directions is that the character of the filter should change as a function of the inhomogeneous coordinate. That is, in the case of wall-bounded flow, the width of the low-pass filter should grow as a function of the distance from the wall,  $x_2^+$ , to reflect the fact that the turbulent eddies increase in size as one moves away from the wall. This problem can be addressed by using the method of proper orthogonal decomposition (POD) to construct low-pass filters that are inhomogeneous in one or more directions. POD provides an optimal set of basis functions for an ensemble of data. It is optimal in the sense that it is the most efficient way of extracting the most-energetic components of an infinite-dimensional process with only a few modes (Holmes et al., 1996).

Consider, for example, time-dependent data on a two-dimensional domain  $\mathbf{x} = (x_1, x_2)$ . In the most general form, the velocity can be expanded as

$$u_i(\mathbf{x}, t) = \sum_k \sum_n a^{(k,n)}(t) \psi_i^{(k,n)}(\mathbf{x}) \quad (6)$$

where  $\psi_i$  is an orthogonal basis for the  $i$ th component of the velocity and the  $a$ 's are the time-dependent coefficients of the expansion. The time-dependent coefficients are extracted using the orthogonality of the basis members. This gives

$$a^{(k,n)}(t) = \frac{1}{L_{x_1} L_{x_2}} \iint u_i(\mathbf{x}, t) \psi_i^{(k,n)*}(\mathbf{x}) d\mathbf{x} \quad (7)$$

where  $L_{x_j}$  is the extent of the domain in the  $x_j$  direction and  $(*)$  denotes the complex conjugate value.

To illustrate the effectiveness of POD as a filtering tool, we will use photographic PIV measurements made in fully-developed turbulent channel flow at a Reynolds number of 5378 based on the bulk velocity and the half-height of the channel (Liu et al., 1991, 1999). This particular flow allows us to reduce the problem to a two-dimensional one and specialize the form of the basis because the streamwise direction ( $x_1$ ) is homogeneous. In this case, we can write  $\psi_i$  as the product of a Fourier basis in the streamwise direction and an optimal, inhomogeneous basis ( $\phi_i$ ) in the wall-normal direction as

$$\psi_i^{(k,n)}(\mathbf{x}) = \phi_i^{(k,n)}(x_2) e^{\frac{i 2 \pi k x_1}{L_{x_1}}} \quad (8)$$

(Note:  $i = \sqrt{-1}$ ). By doing this, we have converted a 2-D problem into a 1-D POD problem in the inhomogeneous, wall-normal direction.

We can now define the POD filter. The total field is separated into a large-scale (filtered) field and a small-scale field

$$\mathbf{u} = \bar{\mathbf{u}} + \mathbf{u}'' \quad (9)$$

where the filtered field is given by

$$\bar{u}_i(x_1, x_2) \equiv \sum_{k=0}^K \sum_{n=0}^N H^{(k,n)} a^{(k,n)} \psi_i^{(k,n)}(x_1, x_2) \quad (10)$$

Here,  $H^{(k,n)}$  is a filter characteristic function that amplifies or attenuates the strength of each POD mode. If  $H^{(k,n)}$  is complex, it also changes the phase of each mode.  $H^{(k,n)}$  is completely analogous to the function  $H(k_1, k_2)$  one would apply to a Fourier representation of a homogeneous signal in  $(x_1, x_2)$ . In the context of POD, the mode number,  $n$ , is analogous to a spatial frequency.

We can write an expression for the filtered field in physical space in the form of a convolution of the original velocity field and a POD filter kernel,  $h$ :

$$\begin{aligned} \bar{u}_i(x_1, x_2) &= \frac{1}{L_{x_1} L_{x_2}} \iint u_j(x'_1, x'_2) h_{ij}(x_1, x_2, x'_1, x'_2) dx'_1 dx'_2 \quad (11) \end{aligned}$$

The filter kernel is a generalized impulse response function. It is given by

$$h_{ij} = \sum_{k=0}^K \sum_{n=0}^N H^{(k,n)} \psi_i^{(k,n)}(x_1, x_2) \psi_j^{(k,n)*}(x'_1, x'_2) \quad (12)$$

Figure 5a shows the Reynolds-decomposed fluctuations for our fully-developed, turbulent channel flow example. Figure 5b illustrates the filtered field obtained when  $H^{(k,n)}$  includes the twelve most-energetic modes, i.e.  $H^{(k,n)} = 1$  for  $k = 0, 1$ , and  $2$ , and  $n = 1, 2, 3$ , and  $4$ . These twelve modes contain 48% of the total energy and 75% of the total Reynolds stress,  $\langle u'_1 u'_2 \rangle$ . The small-scale field is shown in Fig. 5c. Clearly, POD filtering is a very effective scale decomposition in flows with inhomogeneous directions.



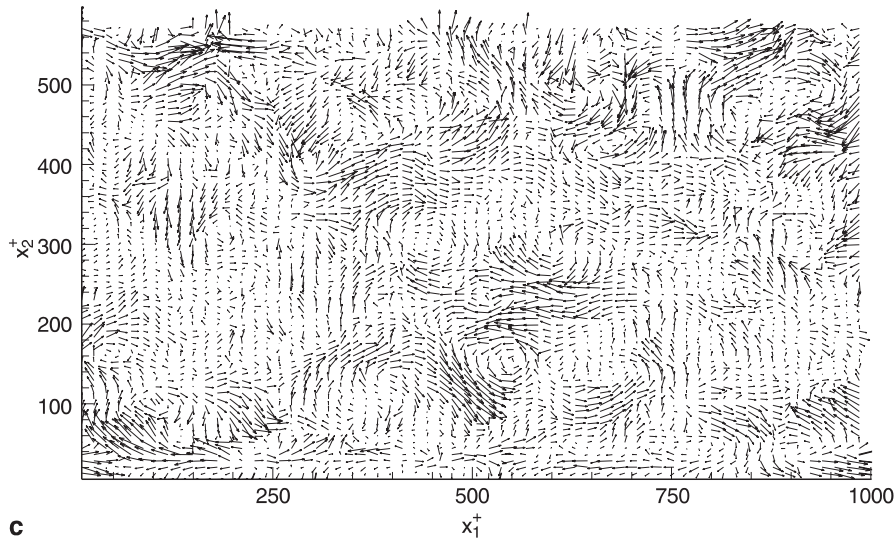
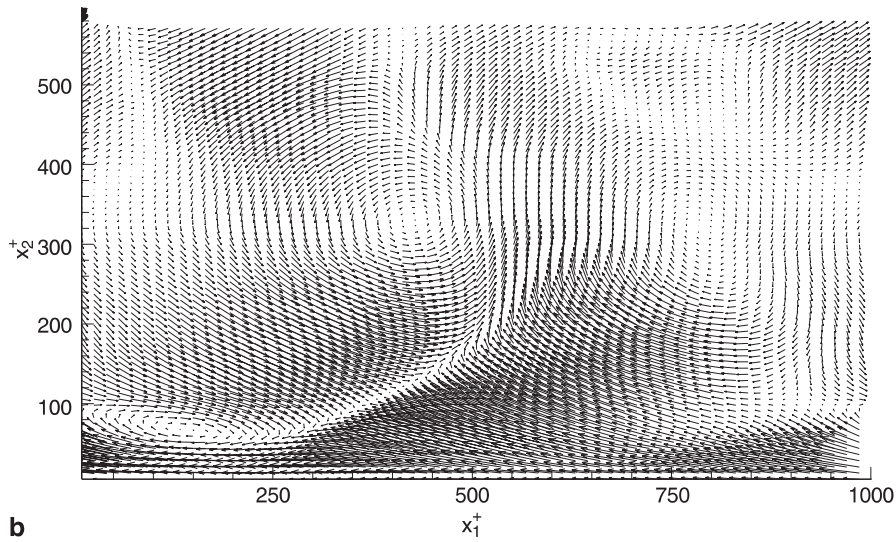
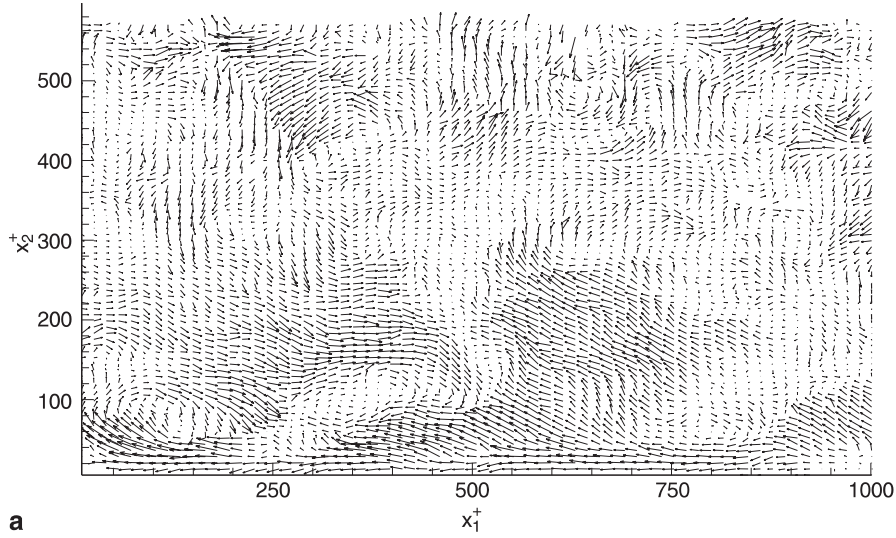


**Fig. 5a-c.** Proper orthogonal decomposition (POD) of fully developed turbulent channel flow. **a** small-scale field obtained by Reynolds decomposition; **b** large-scale POD field ( $k = 0, 1, 2$  and  $n = 1, 2, 3, 4$ ); **c** small-scale POD field

### 3.4

#### Vortex identification

As mentioned previously, vorticity analysis is generally used to identify locations of vortices and to calculate

vortex statistics (size, strength, etc.). Vorticity,  $\omega$ , is defined as

$$\omega \equiv \nabla \times \mathbf{u} . \quad (13)$$



Unfortunately, vorticity not only identifies vortex cores but also any shearing motion present in the flow. In wall turbulence, strong shear layers populate the near-wall region and tend to mask turbulent eddies in vorticity maps. These shearing motions can render the task of computing reliable vortex statistics virtually impossible.

Several groups have proposed new methods of extracting underlying structure from velocity fields which involve critical-point analysis of the local velocity gradient tensor and its corresponding eigenvalues (Chong et al., 1990; Dallman et al., 1991; Zhou et al., 1996, 1999) or the Hessian of pressure (Jeong and Hussain, 1995). In three dimensions, the local velocity gradient tensor will have one real eigenvalue ( $\lambda_r$ ) and a pair of complex conjugate eigenvalues ( $\lambda_{ci} \pm i\lambda_{ci}$ ) when the discriminant of its characteristic equation is positive. When this is true, the particle trajectories about the eigenvector corresponding to  $\lambda_r$  exhibit a swirling, spiral motion (Chong et al., 1990).  $\lambda_{ci}^{-1}$  represents the period required for a particle to swirl once about the  $\lambda_r$ -axis. If the flow is pure shear flow, the particle orbits are infinitely-long ellipses and the orbit period is also infinite, corresponding to  $\lambda_{ci} = 0$ . Thus,  $\lambda_{ci} > 0$  corresponds to shorter, more circular ellipses, i.e. eddies. Zhou et al. (1996, 1999) show that the strength of any local swirling motion is quantified by  $\lambda_{ci}$ , which they define as the swirling strength of the vortex. Vortex identification based on swirling strength is frame independent, meaning that a priori choice of a correct reference frame is not necessary. In addition, it does not reveal regions which contain significant vorticity but are absent of any local swirling motion (i.e., shear layers).

Since PIV fields are usually two-dimensional, the full local velocity gradient tensor cannot be formed. However, an equivalent two-dimensional form of this tensor can be computed in the plane in which the PIV data lies; namely,

$$\underline{\underline{D}}^{2-D} = \begin{bmatrix} \frac{\partial u_1}{\partial x_1} & \frac{\partial u_1}{\partial x_2} \\ \frac{\partial u_2}{\partial x_1} & \frac{\partial u_2}{\partial x_2} \end{bmatrix} \quad (14)$$

where  $(x_1, x_2)$  and  $(u_1, u_2)$  are the streamwise and wall-normal directions and velocities, respectively. In this case,  $\underline{\underline{D}}^{2-D}$  will either have two real eigenvalues or a pair of complex conjugate eigenvalues. Therefore, vortices are easily identified by plotting iso-regions of  $\lambda_{ci} > 0$ .

This analysis was performed on the same pipe flow realization presented earlier. Spatial derivatives were computed using a second-order, central-difference scheme. Iso-regions of swirling strength are shown in Fig. 6a. Swirling strength is noted at all locations where a vortex was identified in the various velocity decompositions (labeled A-I). In addition, the swirling strength analysis reveals four additional vortices that were not identified in any of the velocity decompositions. These new vortices are labeled J-M. Figure 6b shows vorticity contours and swirling strength iso-lines superimposed on one-another. Although vorticity does identify some of the eddies fairly well, it is much noisier than the swirling strength, and it also tends to identify local shear layers present in the field. These shortcomings of vorticity make swirling strength more useful as a means of identifying eddies and calculating reliable vortex statistics.

If one finds the peaks in swirling strength and then performs a local Galilean decomposition in the immediate vicinity of the vortex, the swirling motion around these peaks can be confirmed. This is shown in Fig. 6c. Indeed, swirling motion exists around all of the regions where significant swirling strength exists. This validates our findings in the velocity decompositions where the Kline and Robinson (1989) definition was used to identify eddies. Vortices L and M, which were not seen in the velocity decompositions, have a counterclockwise rotation, while all of the other vortices have a clockwise rotation.

### 3.5

#### Small-Eddy Decomposition

We can continue the swirling strength analysis one step further and actually use it to separate the small-scale structure from the total field. A ‘mean eddy’ can be formed by taking the conditional average of the velocity field around the peaks in swirling strength. This can be written as

$$\mathbf{u}_V = \langle [\mathbf{u}(\mathbf{x} - \mathbf{x}_c) - \mathbf{u}(\mathbf{x}_c)] | \mathbf{x}_c \rangle \quad (15)$$

where  $\mathbf{x}_c$  is the center of the vortex as determined from swirling strength. Figure 7a shows the ‘mean eddy’ found from our single pipe flow realization. The thirteen vortices noted in Fig. 6a were used in this conditional average. The average diameter of these small-scale vortices is 20–40 viscous wall units, depending on the definition of diameter. Figure 7b illustrates how subjective the definition of diameter can be with contours of swirling strength for a typical vortex in the field, along with profiles (streamwise and wall-normal) through the vortex center.

Now, the total field can be filtered using this ‘mean eddy’ as the filter. This is what we refer to as Small-Eddy Decomposition (SED). Just as with the LES decomposition, the total velocity is separated into large-scale and small-scale fields as

$$\mathbf{u} = \bar{\mathbf{u}} + \mathbf{u}'' \quad (16)$$

However, in SED, the filtering kernel is replaced with the conditional average defined in (15). Therefore, the filtered field is given by

$$\bar{u}_1(\mathbf{x}, t) = \int_D u_{V1}(\mathbf{x}' - \mathbf{x}) u_1(\mathbf{x}', t) d\mathbf{x}' \quad (17)$$

$$\bar{u}_2(\mathbf{x}, t) = \int_D u_{V2}(\mathbf{x}' - \mathbf{x}) u_2(\mathbf{x}', t) d\mathbf{x}' .$$

SED provides a true small-scale/large-scale separation because the filter is based upon the small-scale structure embedded in the flow field. Small eddy decomposition is closely related to the technique of matched filtering. Note that if eddies having many different core diameters are present, one should define a set of mean eddies  $\{\mathbf{u}_v\}$  classified according to their diameters. If the elements of  $\{\mathbf{u}_v\}$  are geometrically similar, this will lead to the definition of a wavelet basis function.

Figure 8 shows the small-scale field obtained by SED. Filtering was performed in real space so that the presence of missing vector data could be taken into account. The small-

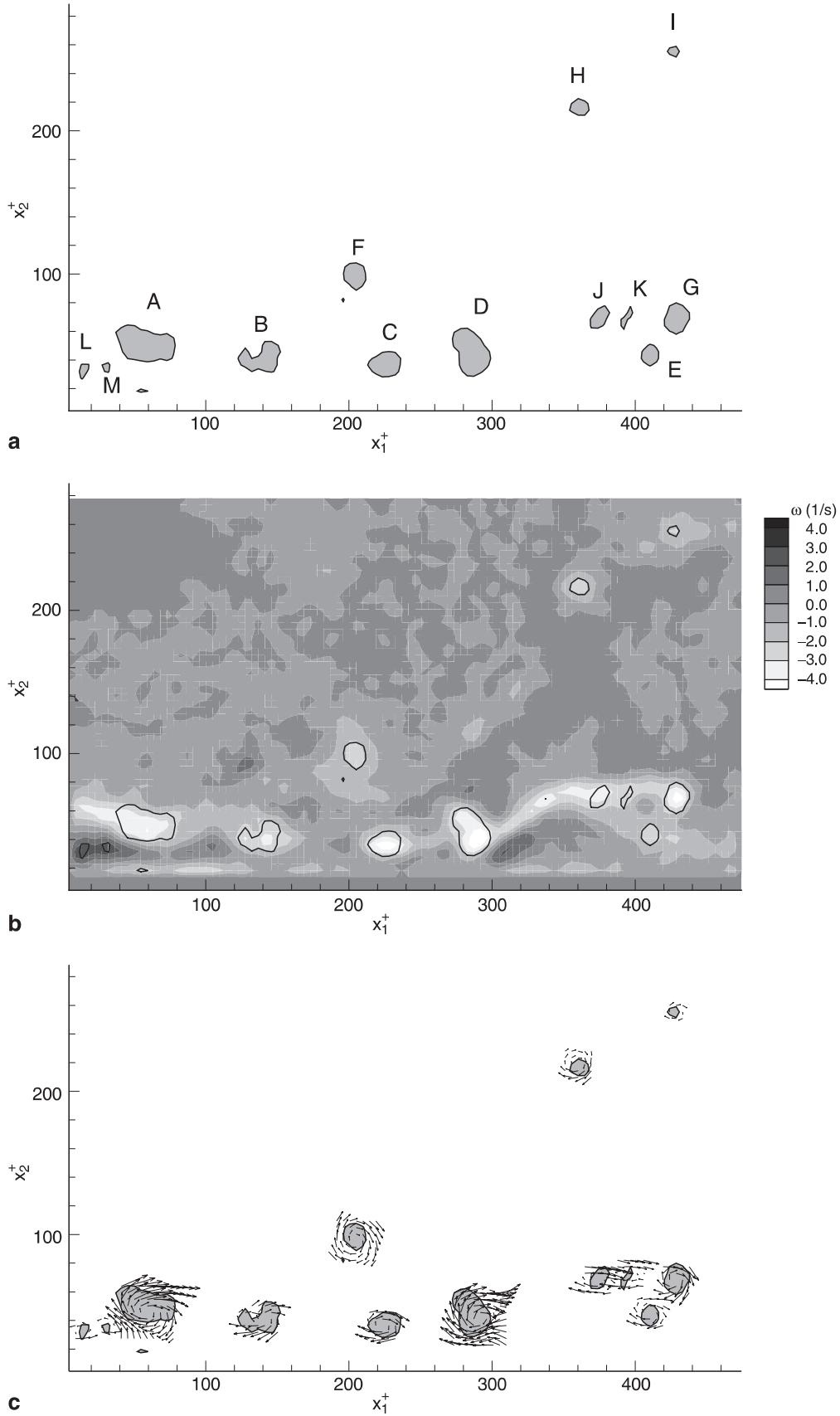


**Fig. 6.** **a** Iso-regions of swirling strength and **b** vorticity (gray-scale) and swirling strength (line) contours for pipe flow. **c** Velocity field (in reference frame of the vortex) around peaks in swirling strength

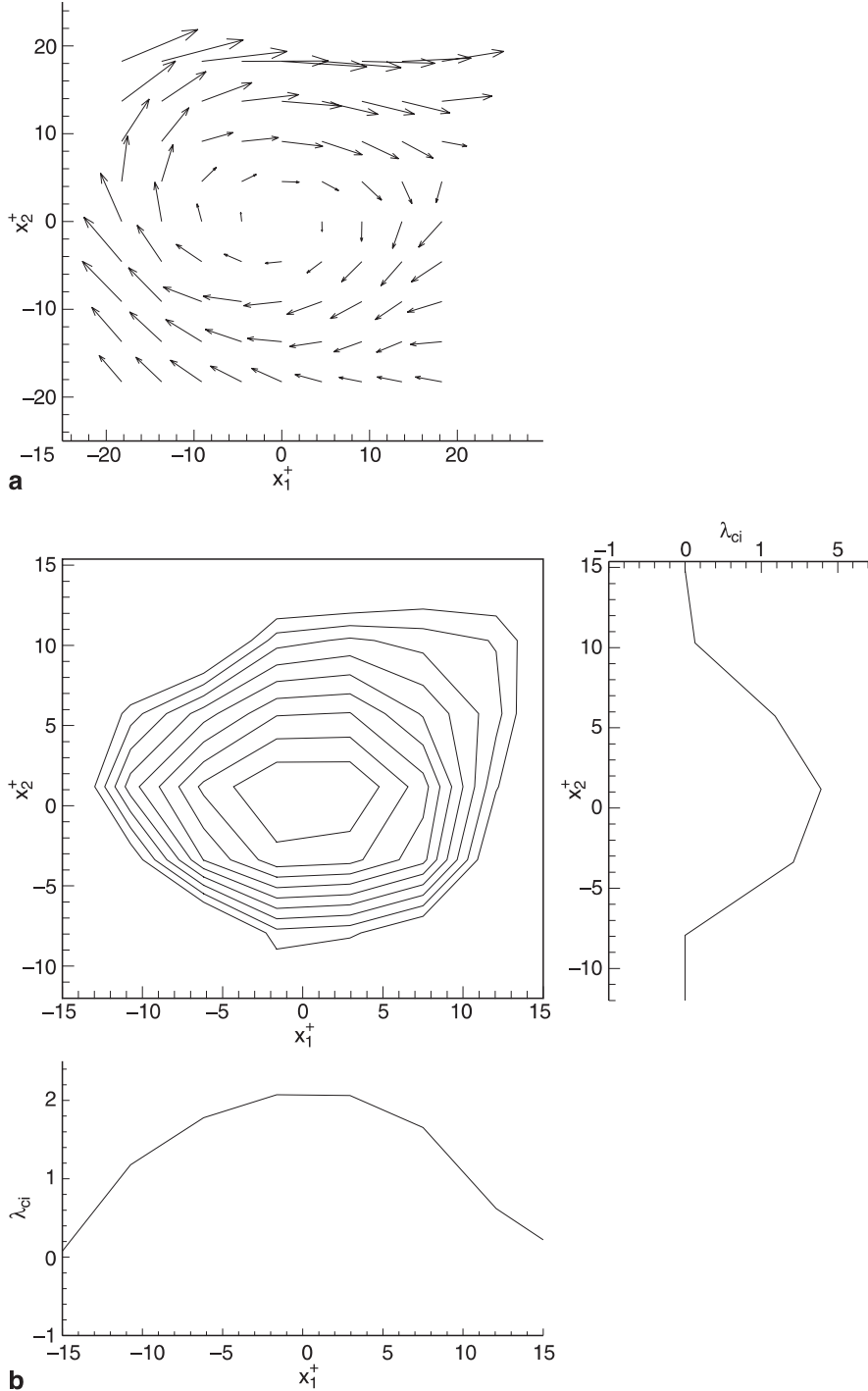


**Fig. 7a,b.** **a** ‘Mean eddy’,  $\mathbf{u}_v(\mathbf{x})$ , found by conditional averaging velocity field based on peaks in swirling strength; **b** Contours of swirling strength for a typical vortex, along with profiles (streamwise and wall-normal) through the vortex center

scale field found by SED appears qualitatively similar to the LES-decomposed small-scale field calculated using a Gaussian filtering kernel. It clearly isolates vortices A-I, the same vortices seen in the other velocity decompositions.

#### 4 Visualization of turbulent stresses

##### 4.1 Reynolds decomposition

When the total velocity ( $\mathbf{u}$ ) and pressure ( $p$ ) are decomposed using Reynolds averaging, the equation governing the mean velocity (for incompressible flow) is

$$\rho \left( \frac{\partial U_i}{\partial t} + U_j \frac{\partial U_i}{\partial x_j} \right) = \frac{\partial}{\partial x_j} \left( -P \delta_{ij} - \rho \langle u'_i u'_j \rangle + \mu \frac{\partial U_i}{\partial x_j} \right) \quad (18)$$

where  $U_i$  is the mean and  $u'_i$  is the fluctuating portion of the  $i$ th component of velocity,  $P$  is mean pressure,  $\rho$  is the density of the fluid, and  $\mu$  is the dynamic viscosity. The Reynolds (turbulent) stresses (second term on the right-hand side of (18)) are a direct result of the velocity decomposition, and they couple the mean and fluctuating velocity equations. The kinetic energy equations (mean and fluctuating) show that the Reynolds stresses are a source of

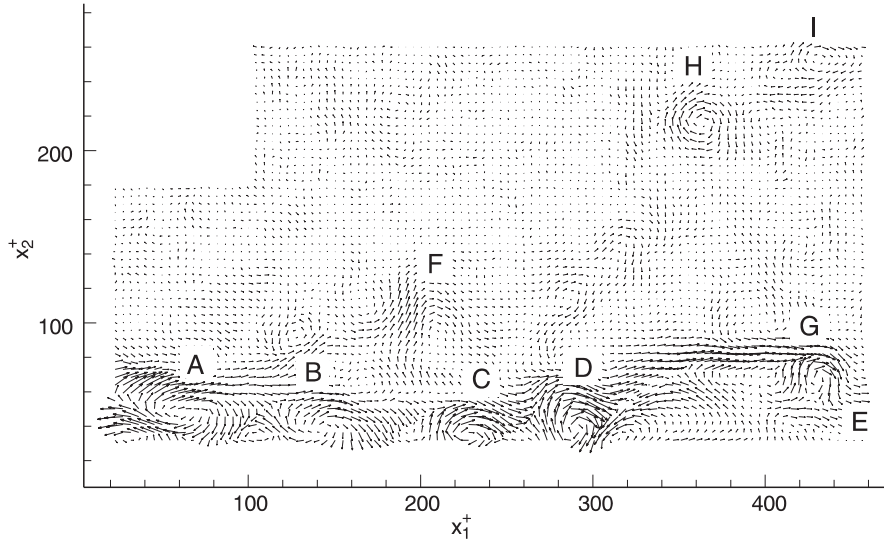


**Fig. 8.** Small-scale velocity field obtained by SED using the ‘mean eddy’ shown in Fig. 7 as the filter

turbulent kinetic energy and a sink for the kinetic energy of the mean. Therefore, these stresses play a crucial role in understanding the underlying dynamics of turbulence.

## 4.2

### Galilean decomposition

In other reference frames, turbulent stresses still exist; however, they may not be precisely the same as the Reynolds stresses. In a Galilean frame, the turbulent stresses are the product of the fluctuations obtained by subtracting a constant convection velocity from the total velocity field. The ensemble-averaged Galilean turbulent stresses are defined as

$$-\langle u_{ci}u_{cj} \rangle \equiv -\langle (u_i - U_{ci})(u_j - U_{cj}) \rangle. \quad (19)$$

If we express the total velocity in terms of a Reynolds-decomposed field, the Galilean stresses can be related to the original Reynolds stresses as

$$-\langle u_{ci}u_{cj} \rangle = -\langle u'_i u'_j \rangle - (U_i - U_{ci})(U_j - U_{cj}). \quad (20)$$

From (20) we conclude that, in general, the Galilean turbulent stresses differ from the Reynolds stresses by a potentially large amount, depending on the relative size of the second term on the right-hand side of (20). However, there are certain classes of flows for which these stresses are identical. For a statistically-convergent dataset obtained from a canonical wall-bounded turbulent flow (boundary-layer or fully-developed pipe or channel flow), the ensemble-averaged turbulent shear stresses (i.e.,  $i \neq j$ ) as seen in a streamwise-translating Galilean frame are identical to the Reynolds stresses since  $U_2, U_3, U_{c2}$ , and  $U_{c3}$  are all zero.

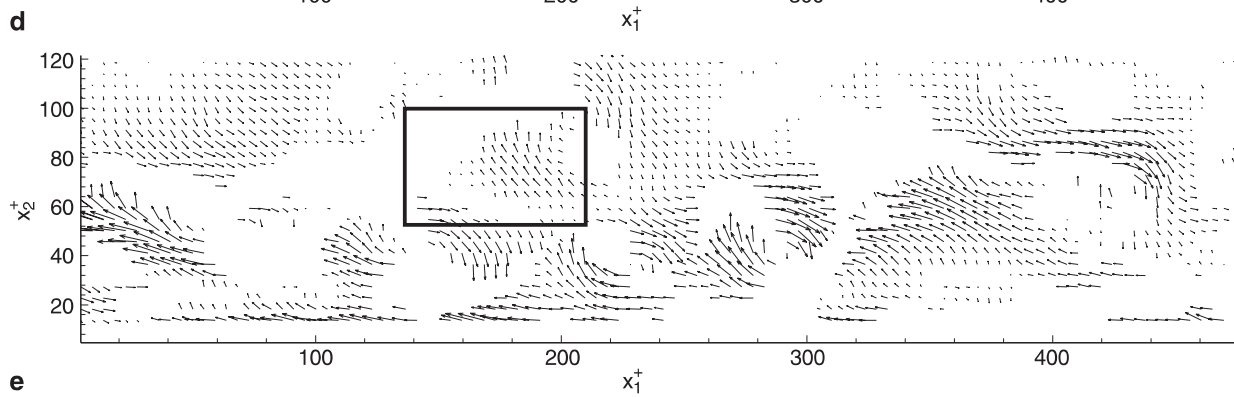
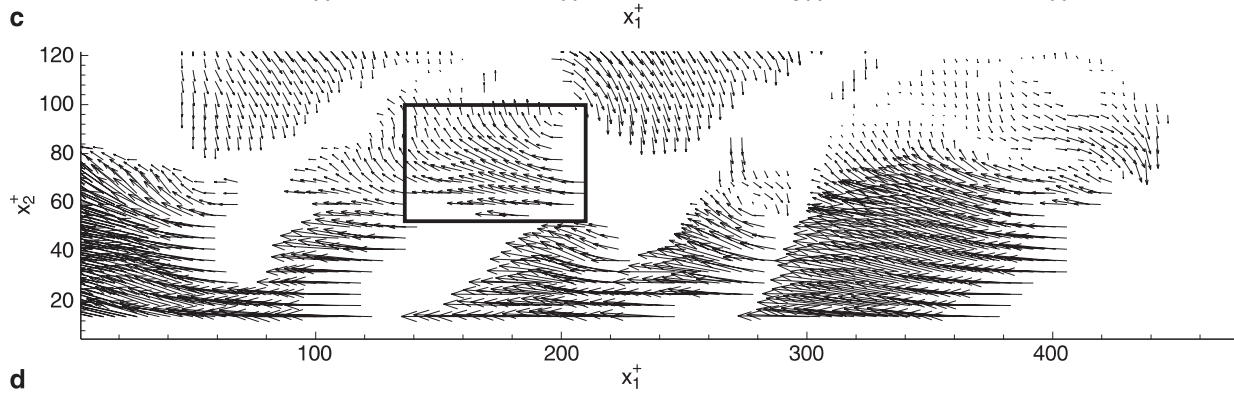
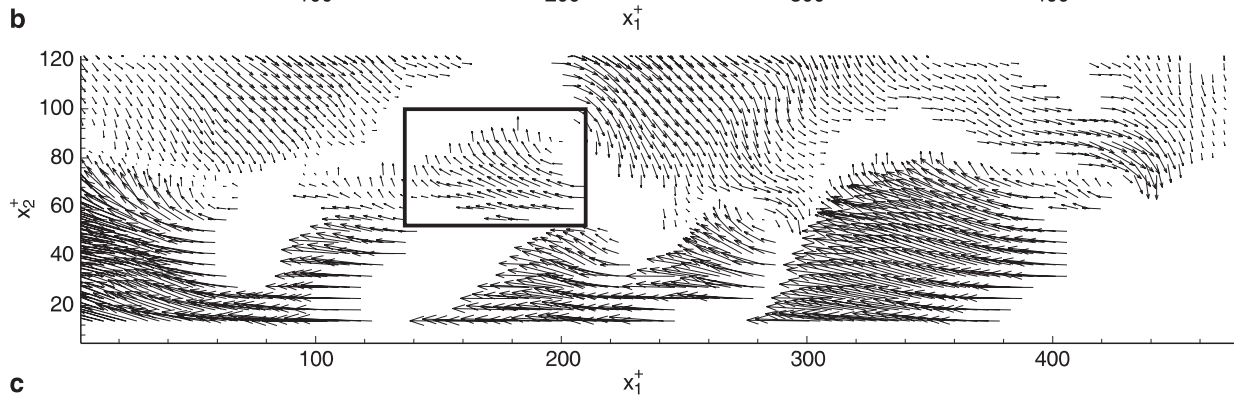
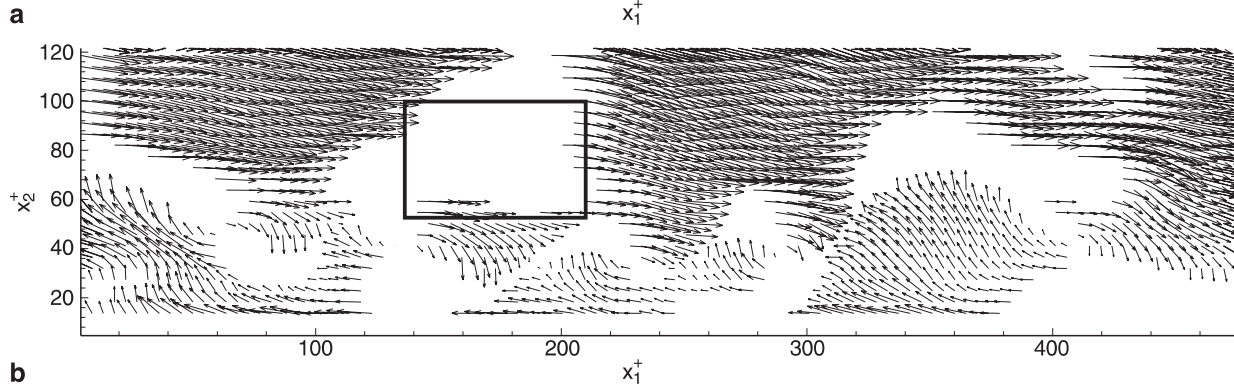
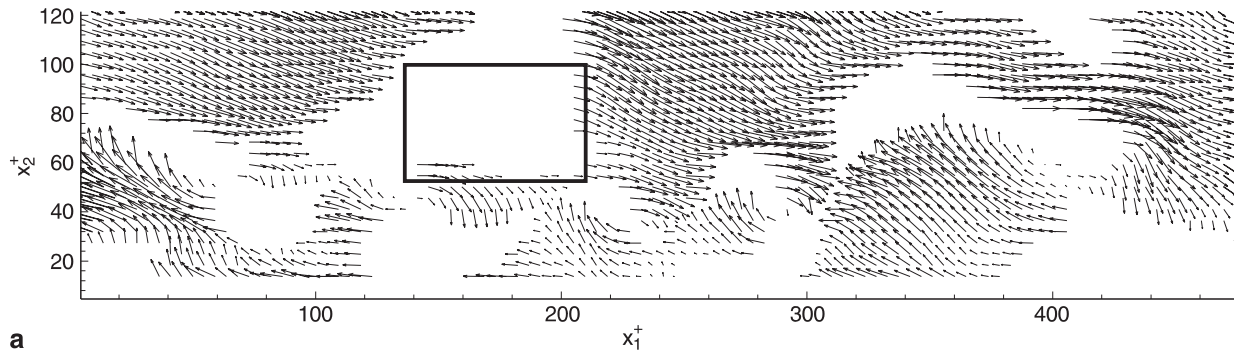
The foregoing observations have a number of implications regarding visualization of turbulent stresses. First, consider visualization of the instantaneous, unaveraged  $Q_2$  and  $Q_4$  turbulent stresses ( $u'_1 < 0, u'_2 > 0$ , and  $u'_1 > 0, u'_2 < 0$ , respectively), as shown in Fig. 9 for our pipe flow example. We choose to focus on the near-wall region because this is where the most intense stress-producing events occur. The patterns of  $Q_2$  and  $Q_4$  events reveal the elements of the flow that act to sustain the

turbulence because they provide energy to the fluctuating field. However, depending on the reference frame in which one views them, these events appear differently, even though their average may be the same for a statistically-convergent dataset. Figure 9a illustrates these stress-producing events for the Reynolds-decomposed field, while Fig. 9b–d illustrate the stress-producing events in three different Galilean frames:  $U_{c1} = 0.5 U_{CL}$ ,  $0.75 U_{CL}$ , and  $0.81 U_{CL}$ . Each is different, and therefore physical conclusions drawn from such data will be frame-dependent. The root cause of this result is the fact that the Reynolds stress tensor is not a true stress created by physical forces, but only momentum transport that has the form of a stress tensor.

A boxed region is highlighted in Fig. 9 to illustrate how the instantaneous stresses-producing events can appear quite differently in the various reference frames. Vortex F resides just to the right of the boxed region. Recall that it was visualized in the second and third Galilean frames (Fig. 3b, c) and the LES-decomposed field (Fig. 4b). This vortex has a clockwise motion and induces a  $Q_2$  event just upstream of it. In the Reynolds-decomposed field (Fig. 9a), this event does not appear. This  $Q_2$  event is also not visible in the first Galilean frame (Fig. 9b). However, in Fig. 9c, d, this  $Q_2$  event is visible because we are visualizing the field in the reference frame of the vortex. This particular example illustrates a very important point: In order to visualize the dynamics induced by a structure embedded in a flow field, one should move in the same frame of reference as the structure. Also, even though the vortex is not visible in the Reynolds decomposed field, it is clearly the source of the stress-producing  $Q_2$  event. Thus, one should not rely on visualization using a single type of decomposition. Instead, it is best to use several frames in order to extract full information about the dynamics of the flow.

**Fig. 9a–e.** Visualization of  $Q_2$  and  $Q_4$  events near the wall in pipe flow for five different decompositions. **a** Reynolds decomposition; **b** Galilean  $U_{c1} = 0.5 U_{CL}$ ; **c** Galilean  $U_{c1} = 0.75 U_{CL}$ ; **d** Galilean  $U_{c1} = 0.81 U_{CL}$ ; **e** LES decomposition





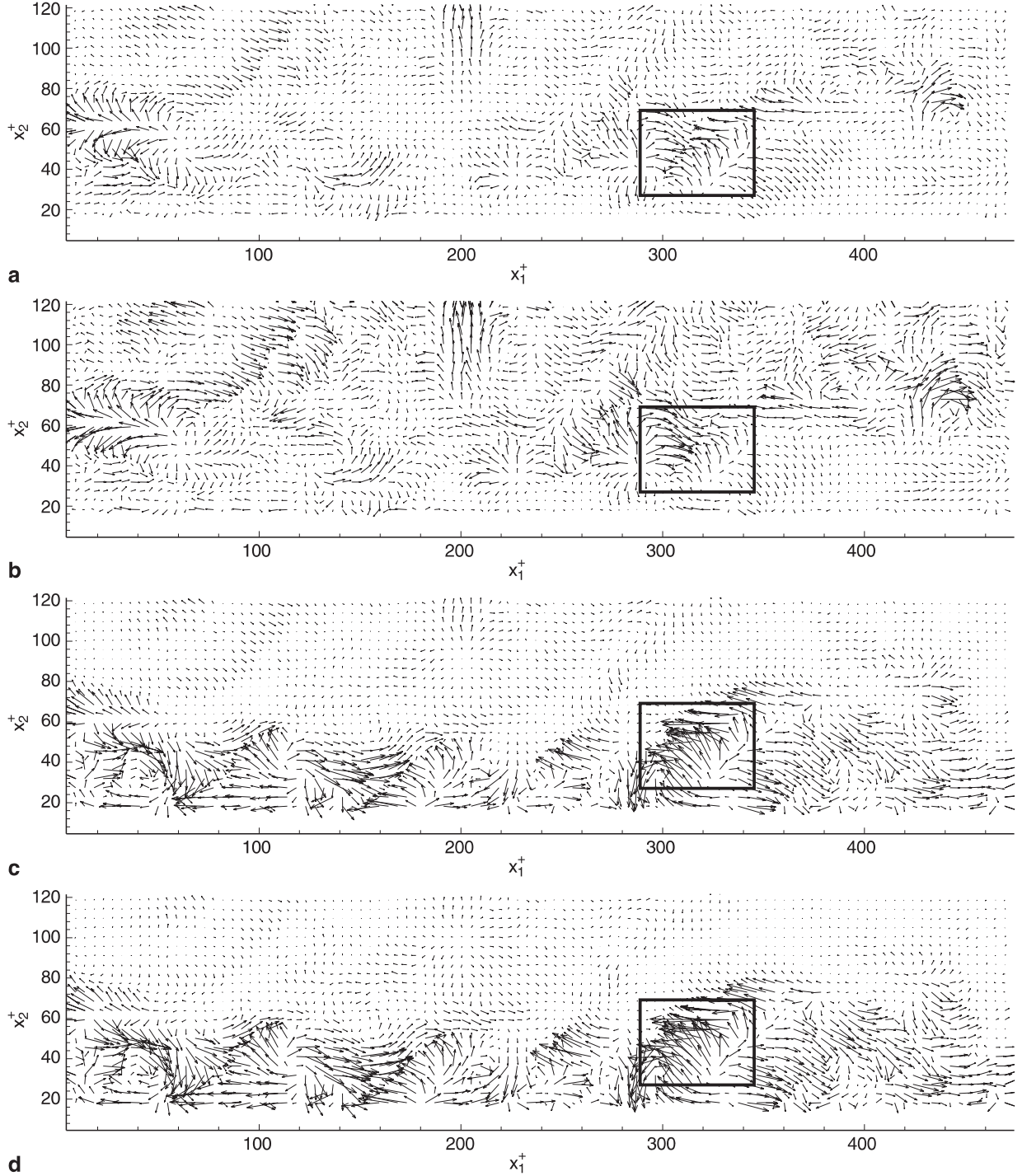


**Fig. 10a–d.** Visualization of net fictitious force imposed by the velocity fluctuations near the wall in pipe flow for Reynolds and Galilean decompositions. **a** Reynolds decomposition; **b** Galilean,  $U_{c1} = 0.5 U_{CL}$ ; **c** Galilean,  $U_{c1} = 0.75 U_{CL}$ ; **d** Galilean,  $U_{c1} = 0.81 U_{CL}$

Finally, for our particular flow,  $x_1$ -averaging the Reynolds-decomposed field  $u'_i u'_j$  (Fig. 9a) or the Galilean frames  $u_{ci} u_{cj}$  (Fig. 9b–d) will give the correct mean Reynolds stresses (except for  $i = j = 1$ ). However, we must emphasize that this is only true in certain situations.

Another approach to understanding the underlying dynamics of the small-scale vortices is to evaluate the net fictitious force fields produced by the turbulent stresses. After all, it is actually the net fictitious force (divergence of turbulent stresses) that directly affects the evolution of the

mean (see Eq. (18)). From (20), the average net fictitious force due to the fluctuations in the Galilean frame is related to the net fictitious force imposed by the Reynolds fluctuations as

$$-\frac{\partial}{\partial x_j} \langle u_{ci} u_{cj} \rangle = -\frac{\partial}{\partial x_j} \langle u'_i u'_j \rangle - (U_j - U_{cj}) \frac{\partial U_i}{\partial x_j} \quad (21)$$

Again, in the most general case, the ensemble-averaged net fictitious force in the Galilean frame is different from that observed in the Reynolds frame. However, for canonical

wall-bounded flows, the second term on the right-hand side of (21) is zero for  $j \neq 1$ . For  $j = 1$ , there are two situations of interest. In boundary-layer flows, the second term is roughly zero, although there is some contribution due to the continual growth of the boundary layer downstream. For fully-developed pipe and channel flow, the second term is identically zero because the flow is homogeneous in the streamwise direction. Therefore, for fully-developed flow in pipes and channels, the mean of the net fictitious force imposed by the fluctuations is equivalent in the Reynolds and Galilean frames.

Two-dimensional instantaneous net fictitious force fields,  $(-\partial(u_{c1}u_{cj})/\partial x_j, -\partial(u_{c2}u_{cj})/\partial x_j)$   $j = 1, 2$ , are shown in Fig. 10a–d for Reynolds decomposition and three Galilean frames. As with the turbulent-stress visualization, we will focus on the near-wall region of the velocity field where the most-intense small-scale vortices reside. The net fictitious force fields, as computed for these different decomposition methods, appear qualitatively similar but quantitatively different. The Galilean fields tend to show regions of larger net force compared to the Reynolds-decomposed result. It is important to note, however, that in this particular flow, line-averaging these net fictitious force fields in the streamwise direction will give equivalent profiles as a function of wall-normal direction. In such cases, the Galilean field of stresses can be interpreted simply.

Now let us focus on the insight that net fictitious force fields provide on the dynamics and interactions of the small-scale vortices in our pipe flow example. In Fig. 10, a region of relatively large net force is boxed for emphasis. This region corresponds to the upstream extent of the  $Q_2$  event imposed by vortices E, G, J and K and the downstream end of the  $Q_4$  event created by Vortex D (see Fig. 6a). This interaction creates an enormous net force not only in the negative streamwise direction, but also away from the wall. This type of intense event produces and sustains the turbulence.

### 4.3

#### LES decomposition

As in the Galilean frame, the turbulent stresses in the LES-decomposed field are not equivalent to the Reynolds stresses. The mean turbulent stresses in the LES frame can be related to the Reynolds stresses as

$$\langle u_i''u_j'' \rangle = \langle u_i'u_j' \rangle + \langle (U_i - \bar{u}_i)(U_j - \bar{u}_j) \rangle - \langle u_i'\bar{u}_j + u_j'\bar{u}_i \rangle. \quad (22)$$

The divergence of the LES-decomposed mean turbulent stresses is

$$\frac{\partial}{\partial x_j} \langle u_i''u_j'' \rangle = \frac{\partial}{\partial x_j} \langle u_i'u_j' \rangle + \left\langle (U_j - \bar{u}_j) \frac{\partial}{\partial x_j} (U_i - \bar{u}_i) \right\rangle - \left\langle \frac{\partial u_i'}{\partial x_j} \bar{u}_j + \frac{\partial \bar{u}_i}{\partial x_j} u_j' \right\rangle. \quad (23)$$

Note that, unlike representation in the Galilean frame, a simple relationship does not exist between the average of the LES-decomposed turbulent stresses and the Reynolds stresses. Figure 9e illustrates the turbulent stress-produc-

ing events in the LES-decomposed field. These events are not as strong as those seen in the Reynolds and Galilean decompositions, although the  $Q_2$  event in the boxed region looks qualitatively similar to the others.

### 5

#### Conclusions

In order to understand the importance of vortex dynamics on the evolution of the large-scale turbulence, one must be able to visualize the vortices and interpret their contribution to the overall flow accordingly. For statistical analysis, Reynolds decomposition is the most appropriate. However, for visualization of vortex structure, other decompositions are shown to be superior. Galilean transformations allow one to not only visualize the core of the small-scale vortices moving at a particular translational velocity, but also the induced motions associated with these vortices (especially near the wall). Despite these advantages, LES decomposition is still the best method for visualizing all of the small-scale vortices in a flow.

Critical-point analysis based on the local velocity gradient tensor leads to a new kinematic quantity called swirling strength (Zhou et al., 1996, 1999). It provides a means of extracting the small-scale vortices from the velocity field, including those which are not visible in the velocity decompositions. Swirling strength also allows one to isolate the velocity field in the vicinity of the vortices in order to assess their contribution to the overall dynamics of the flow. Additionally, it can be used to create a 'small-eddy filter' which permits one to separate the small-scale features of the flow from the larger-scale ones using SED.

Visualization of turbulent-stress-producing events is not as straightforward as visualization of vortices. Instantaneous events (stresses and net fictitious force) appear differently depending on the frame of reference used to visualize the flow. However, the averages of these quantities, in the case of Reynolds and Galilean decomposition, are equivalent for certain flows. This is significant because one could choose to use only Galilean decomposition and still arrive at the same Reynolds-stress and net-fictitious-force statistics, at least for canonical wall flows.

#### References

- Chong MS; Perry AE; Cantwell BJ (1990) A general classification of three-dimensional flow fields. *Phys Fluids* A2: 765–777
- Dallman U; Hilgenstock A; Riedelbanh S; Schulte-Werning B; Vollmers H (1991) On the footprints of three-dimensional separated vortex flows around blunt bodies. AGARD CP-494
- Gursul I; Lusseyran D; Rockwell D (1990) On interpretation of flow visualization of unsteady shear flows. *Exp Fluids* 9: 257–266
- Hama FR (1962) Streaklines in a perturbed shear flow. *Phys Fluids* 5: 644–650
- Holmes P; Lumley JL; Berkooz G (1996) *Turbulence, coherent structures, dynamical systems and symmetry*, Cambridge University Press
- Jeong J; Hussain F (1995) On the identification of a vortex. *J Fluid Mech* 285: 69–94
- Jiménez J; Wray AA; Saffman PG; Rogallo RS (1993) The structure of intense vorticity in isotropic turbulence. *J Fluid Mech* 255: 65–90
- Kline SJ; Robinson SK (1989) Quasi-coherent structures in the turbulent boundary layer. Part I: status report on a community-

- wide summary of the data. In: Kline SJ; Afgan NH (ed) Near Wall Turbulence. Proceedings of Zaric Memorial Conference, pp. 200–217, New York: Hemisphere
- Liu Z-C; Landreth CC; Adrian RJ; Hanratty TJ** (1991) High resolution measurement of turbulent structure in a channel with particle image velocimetry. *Exp Fluids* 10: 301–312
- Liu Z-C; Adrian RJ; Hanratty TJ** (1999) A study of turbulent channel flow with proper orthogonal decomposition. In preparation
- Meinhart CD; Adrian RJ** (1995) On the existence of uniform momentum zones in a turbulent boundary layer. *Phys Fluids* 7: 694–696
- Michalke A** (1964) On the inviscid instability of the hyperbolic-tangent velocity profile. *J Fluid Mech* 19: 543–556
- Robinson SK; Kline SJ; Spalart PR** (1989) Quasi-coherent structures in the turbulent boundary layer. Part II: verification and new information from a numerically simulated flat-plate boundary layer. In: Kline SJ; Afgan NH (ed) Near Wall Turbulence. Proceedings of Zaric Memorial Conference, pp. 218–247, New York: Hemisphere
- Urushihara T; Meinhart CD; Adrian RJ** (1993) Investigation of the logarithmic layer in pipe flow using particle image velocimetry. In: So RMC; Speziale CG; Launder BE (ed) Near-Wall Turbulent Flows, pp. 433–446, Leiden: Elsevier Science Publishers
- Zhou J; Adrian RJ; Balachandar S** (1996) Autogeneration of near-wall vortical structures in channel flow. *Phys Fluids* 8: 288–290
- Zhou J; Adrian RJ; Balachandar S; Kendall TM** (1999) Mechanisms for generating coherent packets of hairpin vortices in channel flow. *J Fluid Mech* 387: 353–359